

Supporting Information for 3D Multi-Energy Deconvolution Electron Microscopy

Michiel de Goede,^{†,¶} Eric Johlin,[†] Beniamino Sciacca,[†] Faysal Boughorbel,[‡] and
Erik C. Garnett^{*,†}

[†]*FOM Institute AMOLF, Amsterdam, 1098 XG, The Netherlands*

[‡]*FEI Company, Eindhoven, 5651 GG, The Netherlands*

[¶]*Current address: University of Twente, Enschede, 7522 NB, The Netherlands*

E-mail: garnett@amolf.nl

A Brief Description of MED-SEM

The multi-energy deconvolution SEM (MED-SEM) technique is a new non-destructive imaging workflow. In this method samples are scanned using a sequence of electron beam energies resulting in back-scattered electron (BSE) signal collection from different depths of the specimen. The resulting image stack, containing subsurface volume information, is processed using a deconvolution algorithm which minimizes the substantial cross-talk between BSE signals emanating from different depths, allowing for the reconstruction of virtual thin sections.

The subsurface emission characteristics of BSEs were studied extensively in the SEM literature.¹ BSE depth profiles showing subsurface emission peaks that depend on the accelerating voltage led to earlier concepts of tomographic imaging in the SEM.^{2,3}

Information depth and resolution conditions for BSE microtomography were studied by Niederig and Rau⁴ and Gostev et al.⁵ with a main focus on subsurface imaging of micro-electronic structures. To achieve layer deconvolution, linear image formation models were as-

sumed⁴⁻⁶ and a number of basic semiconductor layouts were investigated. A key limitation of prior approaches is that they proposed a direct-inversion reconstruction algorithm known to be highly sensitive to noise and outliers. Furthermore, previous BSE tomography schemes relied on parameter tuning by users which limited the application to a very small number of layers, and prevented the automation of the imaging process. These considerations restricted the applicability of BSE tomography, an otherwise high potential non-destructive 3D imaging technique in the SEM.

To address these limitations, an adapted computational approach is presented. It forms the basis of the MEDSEM method which is applied here in an imaging regime that better approximates a linear model. A useful observation enabling MEDSEM was that in practice most of the detected BSEs emerge from a relatively thin column localized on the axis of the primary beam. We observed that this effect can result in surprisingly good lateral resolution for subsurface layers.

The current MEDSEM workflow uses no prior knowledge of the BSE point spread function (PSF). It instead employs blind source separation (BSS) techniques⁷ to deconvolve signals

from different depths. Relevant Poisson noise models that characterize the imaging process are also taken into account.

The first step in the MEDSEM workflow is the acquisition of a BSE image stack of the regions of interest in the sample. The acquisition step uses SEM auto-adjustments (focus/stigmatism, contrast, brightness) for consistent image quality across the sequence.

This is followed by image stack registration which needs to be done with high accuracy to enable good results with subsequent reconstruction algorithms. The latter algorithms rely on estimating pixel-to-pixel statistical dependencies across the layers.

For reconstructing 3D volumes from the BSE stacks a deconvolution algorithm based on blind source separation (BSS) techniques was developed. BSS algorithms are used to deconvolve multiple linearly mixed signals in various applications.⁷ The deconvolution was restricted to the Z dimension (depth) only based on the observation that the subsurface X-Y spread of the detected BSEs is limited for a range of useful imaging conditions. The off-axis emission was assumed to represent a weak background signal that does not substantially affect resolution. Such laterally confined PSF model was observed in the work of Hennig and Denk⁸ and in our own Monte Carlo simulations. An extension of the PSF footprint to a full 3D volume is being developed for deeper sample probing where the lateral spread will become more significant.

The MEDSEM Deconvolution Algorithm

The image formation of each BSE image Y_n is modeled as:

$$Y_n = H_n * O \quad (\text{S2})$$

Which represents the convolution of the imaged volume O with a beam-energy dependent point spread function H_n . The aim of the reconstruction technique is to recover an estimate of the volume O from the acquired BSE image stack $\{Y_n\}_{n=1,.,N}$. The main difference with conven-

tional deconvolution techniques, such as those used in 3D fluorescence microscopy, is the use of a variable PSF that depends on beam energy. This PSF will account for the signal coming from the both deeper and shallower layers of the sample. One can formulate the variable-kernel deconvolution task using a conventional Bayesian restoration framework. The probability of the sought spatial variable O given the acquired images Y_n is $\Pr(O|Y_n)$. While $\Pr(O)$ is defined as the prior probability associated with O representing our knowledge about the structure to be reconstructed, and $\Pr(Y_n)$ as the probability of the acquired images. This latter is a constant given that the images Y_n are observed. Using Bayes rule we have

$$\Pr(O|Y_n) = \frac{\Pr(Y_n|O) \Pr(O)}{\Pr(Y_n)} \quad (\text{S3})$$

In the Bayesian framework our problem can be expressed as the following maximization task:

$$\hat{O} = \operatorname{argmax}_{O \geq 0} \{\Pr(O|Y_n)\} \quad (\text{S4})$$

Where we need to enforce the non-negativity of the variable \hat{O} in order to obtain a physically meaningful estimate \hat{O} . It is common to minimize the log-likelihood function to simplify the calculations:

$$\hat{O} = \operatorname{argmin}_{O \geq 0} \{-\log(\Pr(O|Y_n))\} \quad (\text{S5})$$

Our electron detection is well modeled by a Poisson process. At each voxel x in the 3D grid Ω the image is assumed to be formed by the realization of independent Poisson processes. This leads to:

$$\Pr(O|Y_n) = \prod_{x \in \Omega} \frac{((H_n * O)(x))^{Y_n(x)} \exp(-(H_n * O)(x))}{Y_n(x)!} \quad (\text{S6})$$

To recover the volume O we need to minimize the criterion

$$\begin{aligned} J(O|Y_n) &= -\log(\Pr(O|Y_n)) \\ &= \sum_{x \in \Omega} ((H_n * O)(x)) - Y_n(x) \cdot \log((H_n * O)(x)) \end{aligned} \quad (\text{S7})$$

Using fixed-point iterative derivation⁹ the positivity-constrained minimization problem (S5) can be solved using the following scheme:

$$O^{l+1}(x) = O^l(x) \cdot \left(\frac{Y_n(x)}{(H_n * O^l)(x)} * H_n(-x) \right) \quad (\text{S8})$$

This algorithm is a variant of the well-known expectation maximization maximum-likelihood (EMML) approach.^{10,11}

In our case the iterative algorithm needs to be sequentially used for all kernels H_n associated with the different PSFs. Convergence can be assessed empirically or based on other criteria such as the relative change in the variables. In practice, we need to recover or fine-tune the values of the unknown PSF kernels H_n as well. Therefore, we are using alternate minimization O and H_n . We then obtain the following algorithm:

$$H_n^{l+1}(x) = H_n^l(x) \cdot \left(\frac{Y_n(x)}{(H_n^l * O^{l+1})(x)} * O^{l+1}(-x) \right) \quad (\text{S9})$$

The variables O and H_n can have random initializations or can start from some rough initial model. In our work the deconvolution mostly reduced to unmixing the layers in the depth as explained earlier.

PSF Profiles

As described in the previous section, the blind source separation works by computing the maximum likelihood of the convolution of the estimated physical structure and a point spread function for each electron energy. It can be useful to examine the determined point spread functions to ensure that the deconvolutions are proceeding in a physically plausible manner.

In Fig. S1 we show the calculated H_n PSF

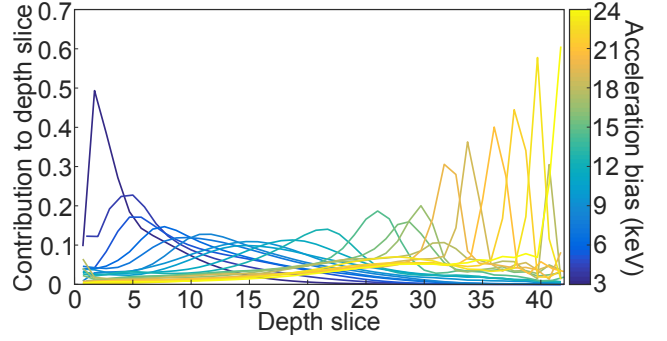


Figure S1: Determined point spread functions (PSFs), H_n , showing the contribution of collected emission per depth slice layer for each electron energy. The functions are normalized so that for each slice the contribution of all PSFs sum to one.

values for each electron energy as their contribution to the determined depth slices to the core-shell nanowire example from the main text (Fig. 2). The determined PSFs appear quite similar to those depicted schematically in Fig. 1 of the main text – higher electron energy PSFs contribute more to deeper depth slices, and, up to ~ 15 keV increasingly broaden as well. Past this point, however, the PSFs appear to be increasing in sharpness.

While this sharpness of high energy PSFs may appear odd at first, it actually entirely expected: The normalization of Fig. S1 shows the relative contribution of each PFS to the estimates of the physical depth slices. For slices at depths past the center of the sample, each deeper slice has fewer PSFs contributing to the composition of the slice (as lower energy electrons do not probe these depths), and thus the contribution of the present PSFs necessarily becomes larger, increasing the sharpness of the increasing slice depth. Despite the sharp appearance, careful inspection shows the contribution to preceding layers of the higher energy electron PSFs is still significant, as expected.

The reconstructions (or at least the convergence time) could possibly be improved slightly by modifying the initial guesses of the PSF shapes, but this would require some *a priori* knowledge of the energy range and interaction depths for the materials investigated. As this study focuses on the ability of the MEDSEM

technique to operate without any input other than a BSE image stack, we believe it is quite encouraging that the PSF profiles fit their expected shapes.

Resolution

The achievable resolution in MEDSEM depends strongly on a number of factors, including the scanning electron microscope used, the quality of the focus/stigmation adjustments between energy modifications, the alignment (registration) of the BSE image stack, and the number and range of energies measured.

For the setup and measurements here, the shape resolution of the nanowire samples in Fig. 3 provide the example with the smallest features. Compared to the FIB cross cuts, dimensions of the nanowire cross sections are fairly accurate – the left nanowire is $35\text{ nm} \times 45\text{ nm}$ in the FIB measurement, and approximately $36\text{ nm} \times 48\text{ nm}$ in the MEDSEM reconstruction. Similarly, the right nanowire is $51\text{ nm} \times 29\text{ nm}$ in FIB and approximately $56\text{ nm} \times 34\text{ nm}$ in the MEDSEM reconstruction. The 10 nm thick gold sheet is resolved well in both.

The lateral resolution appears limited by shifts in the vertical stacking of the layers – at a pixel size of 4 nm , a one pixel misalignment between two layers would give a 4.5 nm error in the relative positions of features. The alignment is thus performed on higher resolution raw images to minimize these effects. The depth resolution is more difficult to define, as the “flattening” aberrations cause there to be more of an uncertainty limit than resolution limit to the reconstructions: two distinct structures may be resolvable, but their relative position to other structures may be uncertain. However, given ability to resolve features of 10 nm , and the accuracy of the nanowire reconstruction dimensions, we estimate that for the investigations here, the lateral resolution seems to be $\sim 5\text{ nm}$, and the depth resolution to be $\sim 10\text{ nm}$.

References

- (1) Reed, S. *Journal of Microscopy* **1999**, *193*, 268–268.
- (2) Seiler, H. *Scanning Electron Microscopy* **1976**, *1*, 9–16.
- (3) Wells, O.; Savoy, R.; Bailey, P. *Proceedings of Asilomar Conference* **1982**, 287–298.
- (4) Niedrig, H.; Rau, E. *Nuclear Instruments and Methods in Physics Research Section B: Beam Interactions with Materials and Atoms* **1998**, *142*, 523–534.
- (5) Gostev, A.; Matvienko, A.; Rau, E.; Savin, V.; Savin, D. *Bulletin of the Russian Academy of Sciences. Physics* **1998**, *62*, 475–480.
- (6) Gostev, A.; Ditsman, S.; Lukyanov, F.; Orlikovskii, N.; Rau, E.; Sennov, R. *Instruments and Experimental Techniques* **2010**, *53*, 581–590.
- (7) Comon, P.; Jutten, C. *Handbook of Blind Source Separation: Independent Component Analysis and Applications*; Academic press, 2010.
- (8) Hennig, P.; Denk, W. *Journal of Applied Physics* **2007**, *102*, 123101.
- (9) Lanteri, H.; Roche, M.; Aime, C. *Inverse problems* **2002**, *18*, 1397.
- (10) Shepp, L. A.; Vardi, Y. *Medical Imaging, IEEE Transactions on* **1982**, *1*, 113–122.
- (11) Richardson, W. H. *Journal of the Optical Society of America* **1972**, *62*, 55–59.